

pubs.acs.org/JPCC Article

# Salt-Induced Liquid—Liquid Phase Separation and Interfacial Crystal Formation in Poly(N-isopropylacrylamide)-Capped Gold Nanoparticles

Alejandra Londoño-Calderon, Wenjie Wang, Jack J. Lawrence, Wei Bu, David Vaknin, and Tanya Prozorov\*



Cite This: J. Phys. Chem. C 2021, 125, 5349-5362



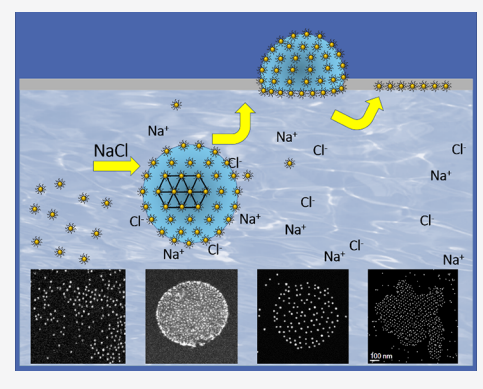
**ACCESS** 

Metrics & More

Article Recommendations

s Supporting Information

ABSTRACT: We report on the dynamic response of aqueous solution containing poly(N-isopropylacrylamide)-capped gold (pNIPAM-capped Au) nanoparticles to the introduction of NaCl. The addition of NaCl increases the density of the solution and prompts the liquid—liquid phase separation process, confining the polymer to a lower-density salt-deficient aqueous phase. As the pNIPAM-occupied aqueous phase becomes excluded from the higher-density NaCl-rich bulk solution, the pNIPAM-capped Au nanoparticles follow liquid—liquid phase separation and reside on the surface of the formed pNIPAM-filled globes at the interface between the NaCl-rich bulk solution and the pNIPAM-containing solution, exhibiting a hexagonal packing with interparticle distance of ~23 nm. Driven by the minimization of hydrophobic interactions, the buoyant Au-decorated globular assemblies filled with aqueous pNIPAM solution escape to the air/water interface, collapse at the interface, and form planar hexagonal crystalline domains of different sizes, depending on NaCl



concentration. At low NaCl concentrations, the collapse of the Au-decorated aqueous pNIPAM-filled globes at the air/water interface produces an interfacial two-dimensional (2D) hexagonal lattice of pNIPAM-capped Au nanoparticles with an interparticle distance of 25–27 nm. The increase in NaCl concentration leads to a formation of smaller globes escaping to, and collapsing at the air/water interface and yielding smaller two-dimensional hexagonal domains.

# 1. INTRODUCTION

Amphiphilic polymers are widely used in material synthesis. Such polymeric systems can form a variety of hierarchical nanostructures, making them attractive for use in stimuli-responsive bioinspired synthesis. In designing such complex, functional nanostructures, it is important to have a high level of control over the individual system components, and doing so requires an understanding of mechanisms and processes involved in stimuli-responsive, self-, or directed nanoparticle assembly. Despite significant progress, these mechanisms often remain elusive.

Salt-induced assembly of nanoparticles grafted with amphiphilic polymers is a relatively straightforward technique. An aqueous system of a neutral amphiphilic polymer and salt can undergo a biphasic separation subject to the molecular weight of the polymer, salt concentrations, and pH value. Lattice symmetry and interparticle distance can be easily tuned using a versatile toolbox offered by selecting various grafting polymers and salt ions. Although there are several studies reporting on salt-inducing polymer—nanoparticle assembly of one- to three-dimensional lattices at the air/water interface, little is known about the processes taking place in liquid and their progression toward the assembly of crystals at the interface.

An example of a relatively well-established area is the temperature- and salt-induced assembly of poly(N-isopropylacrylamide)—pNIPAM, 1-3 in which a coil-to-globule transition (CGT) is observed at the lower critical solution temperature (LCST),4,5 the latter being highly sensitive to the presence of ions in solution. pNIPAM is said to resemble the cold denaturation of globular proteins, and for this reason, pNIPAM is considered a model for understanding the effects of specific ions on a number of biologically relevant reactions, ranging from the solubility and stability of proteins to enzymatic action in crowded macromolecular environments, to creating smart devices incorporating pNIPAM and DNA functionalities. 1,6-10 The CGT in pNIPAM is often viewed by utilizing a combination of theoretical approaches devised to rationalize the occurrence and the mechanism of cold protein denaturation, using an assumption that the effective size of

Recived: December 19, 2020 Revised: February 13, 2021 Published: March 1, 2021





bound vs loose water molecules depends on the temperature. <sup>6,7</sup> This theoretical effort is complemented by a growing number of experimental studies, with the general consensus that the globular collapse transition is "entropy-driven" by decreasing the solvent-excluded polymer shell to maximize the translational entropy of water molecules and ions and minimize the hydrophobic interactions. <sup>11–18</sup> The reduction in the solvent-excluded volume plays a major role when a polymer chain passes from a swollen conformation to a collapsed one, which corresponds to an increase in the translational entropy of water molecules. Such a mechanism is further favored by NaCl addition. From the point of view of bioinspired synthesis, the use of readily available pNIPAM systems offers a number of exploitable properties based on thermal cycling in a moderate temperature range. <sup>13,19–22</sup>

The use of stimuli-responsive polymer grafted onto inorganic nanoparticles has been recently explored for the controlled self-assembly into one-, two-, or three-dimensional (1D, 2D, and 3D) lattices. 23-29 The formation of controlled lattices from polymer-grafted nanoparticles provides collective properties different from those of individual nanoparticles. 28,30 The formation of the crystalline lattice of polymer-grafted nanoparticles at an air/water interface can be triggered by a simple addition of salt.<sup>24,30-34</sup> However, the dynamics involving pNIPAM-driven nanoparticle assembly is still not fully understood, with the majority of experimental data available from scattering techniques and NMR.35-38 These data provide important information on interparticle interactions and the formation of equilibrium mesostructured and long-range structures in solution. <sup>24,29,33,34,39</sup> It is possible to reconstruct the self-assembly and stimuli-responsive processes taking place in solution over a wide range of sizes and perform averaging over the volume and time. Often, the reconstructed scenario of the process is the only picture of the nanoparticle assembly process available to researchers, sometimes accompanied by the "start and finish" transmission electron microscopy (TEM) snapshots of nanoparticles at the beginning and end of the process. Such an approach is valid, and it provides important experimental insights into the plethora of processes; however, it largely leaves out the dynamic processes involved in the nanoparticle assembly process, including the formation of intermediate, short-lived

Using dynamic liquid-phase scanning transmission electron microscopy (LP-STEM) imaging, it is possible to study nanoparticle nucleation and growth, 40 assembly kinetics in suspension, 41,42 track the movement and translation of nanoparticles in liquid, 42-44 and assess their dynamic response to external stimuli. 44,45 The ability to follow processes of interest at the nanometer scale in liquid makes LP-STEM an excellent technique uniquely suitable for exploring the nature of the formation of nanoparticle assemblies. 46-48 In this report, LP-STEM is used to examine the behavior of the pNIPAMcapped Au nanoparticle system upon the addition of NaCl. A salt-induced liquid/liquid phase separation in the pNIPAM solution is observed as pNIPAM is driven to form globular assemblies decorated with pNIPAM-capped Au nanoparticles in response to CGT triggered by the introduction of NaCl to the system. Furthermore, we explore the effect of NaCl in the formation and quality of 2D lattices at the air/water interface with scattering techniques, and with the conventional STEM once the lattice is collected and imaged in a dry state. With both pictures at hand, we propose a mechanism of NaClinduced liquid/liquid phase separation and formation of 2D nanoparticle interfacial crystal lattices in a pNIPAM-capped Au nanoparticle system.

# 2. METHODS

**2.1. Materials.** All chemicals in this report were used without further modification unless otherwise noted. Au nanoparticle suspensions with a nominal diameter 10 nm were purchased from Ted Pella (Redding, CA). The monothiol-terminated poly(N-isopropylacrylamide) powder with a molecular weight of 6 kDa was purchased from Sigma-Aldrich. All aqueous solutions were prepared with nanopure water passed through the E-Pure Ultrapure Water Purification System (18.2 M $\Omega$ -cm) (Thermo Scientific). The procedure to graft pNIPAM onto Au nanoparticles is described elsewhere. The final concentration of pNIPAM-capped Au nanoparticles used for X-ray characterization was determined by UV—vis analysis at 20.0 nM concentration. Continuous carbon film grids, Cu 400 mesh, used in this study, were purchased from Ted Pella (Redding, CA).

2.2. Fluid Cell Assembly and the Liquid-Phase Highangle Annular Dark-field (HAADF)-STEM Characterization of the System. The liquid-phase STEM (LP-STEM) imaging in situ was carried out using a commercial continuous flow fluid cell holder platform (Hummingbird Scientific, Lacey, WA). Silicon nitride chips were UV/O<sub>3</sub> plasma-cleaned using a ProCleaner (Bioforce Nanosciences, Ames, IA) for 20 min prior to use to ensure contaminant removal. The liquid-loaded cell was formed by sandwiching two SiN-coated silicon chips with a 50  $\times$  200  $\mu$ m<sup>2</sup> electron transparent 50 nm thick SiN opening etched from the center, forming an imaging window. In our experiments, either both of the SiN windows were square windows and were lacking the 100 nm SU-8 spacers to ensure that the minimal thickness of the liquid layer could be obtained during the imaging or both SiN windows had a 100 nm SU-8 spacer, to obtain a nominal 200 nm liquid layer. During the initial LP-STEM imaging of the pNIPAM-capped Au nanoparticle system in the presence of NaCl, only the square SiN UV/O<sub>3</sub> plasma-cleaned window chips were used. In these experiments, one square chip was placed on the holder and charged with 0.3 µL of solution pNIPAM-capped Au nanoparticles after the addition of NaCl, and immediately topped with a second plasma-cleaned square chip with a similar window orientation, with the excess of the liquid wicked away with the thin strip of a lens paper. Following the aligning of the windows, the two chips were sealed in a holder. In all remaining experiments, one 100 nm spacer chip with a window oriented perpendicularly to the channel was charged with 0.3  $\mu$ L of solution pNIPAM-capped Au nanoparticles after the addition of NaCl, placed on the holder and topped with a second 100 nm spacer chip with a similar window orientation. After aligning the windows, the two chips were sealed to prevent evaporation of the liquid. Following the cell assembly and vacuum check, the sealed holder was inserted into the microscope and allowed to equilibrate for ~20 min before imaging in the HAADF-STEM mode. The experiments with 500 mM NaCl were carried out by delivering the NaCl solution into the fluid cell with the syringe pump using a pumping speed of 2.5  $\mu$ L/min, with the total volume of NaCl solution delivered into the cell 16  $\mu$ L. The STEM images were recorded using a FEI Tecnai G<sup>2</sup> F20 STEM equipped with a Tridiem Gatan image filter operating at 200 kV in high-angle annular dark-field (HAADF) STEM

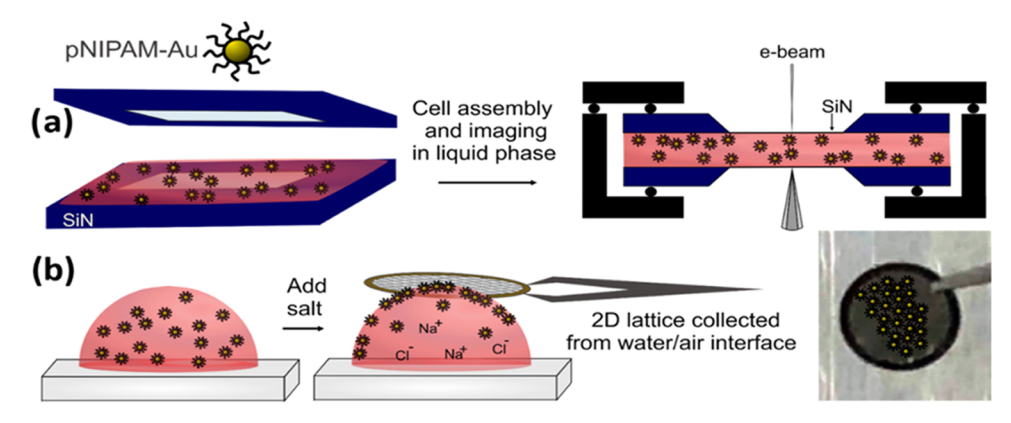


Figure 1. Schematics of the methods used for the characterization of (a) pNIPAM-capped Au nanoparticles in aqueous phase with and without salt, and (b) salt-induced phase separation at the air/water interface in a dry state.

mode. We worked in the HAADF-STEM mode with condenser aperture C2 = 70  $\mu$ m and a camera length of 87 mm, with the data acquisition carried out primarily at magnification range  $M = 40\,000-56\,000\times$  and using a spot size 10. Data analysis was performed with TEM Imaging & Analysis (FEI) software (version 4.12, built 2120), Digital-Micrograph (Gatan) software version 3.22.1461.0, Origin 2018, and ImageJ. The radial distribution function (RDF) was calculated with ImageJ using the macro Radial Distribution Function provided by Michael Schmid & Ajay Gopal. In this case, the RDF is defined as the radial profile of the autocorrelation in binarized imaged above a threshold. Nanoparticles near the edge are avoided to reduce edge effects. The position of the particles for histogram construction was obtained using a Delaunay triangulation. Voronoi's constructions were done using Scipy, Skimage, and Matplotlib packages in Python 3.7. Continuous capture movies were recorded for approximately 3 min using a freeware screen grabber, AutoScreenRecorder (Wisdom Software), that recorded the images at a rate of 8 frames per second. Video editing was performed with BigaSoft Total Video Convertor (Bigasoft 6).

**2.3.** Transfer of Interfacial pNIPAM-Capped Au Nanoparticles to the Grid. A microvolume of pNIPAM-capped Au nanoparticles with NaCl was prepared by placing 2  $\mu$ L of aqueous pNIPAM-capped-Au colloid on a clean hydrophobic corning cover glass 1 1/2 22 × 22 mm². To the surface of the droplet, a volume of 4  $\mu$ L of NaCl (for a final concentration of 5, 50, 250, and 500 mM NaCl and ~10 nM nanoparticles) was added and left to mix for 1 min. The water/air surface of the droplet was gently touched with a continuous carbon film grid (carbon film facing down) for 30 s. The hydrophobicity of the substrate and the grid allowed collecting material from the surface of the droplet with a minimal amount of liquid transferred to the grid.

**2.4. Synchrotron X-Ray Experiments.** The synchrotron X-ray experiments were carried out on a liquid surface spectrometer at ChemMatCars (beamline ID-15) of the Advanced Photon Source (APS), Argonne National Laboratory. The incident X-ray energy was 10 keV. The instrumental information is provided in ref 49. The experimental setup for X-ray measurements is provided in ref 32. The results shown here are for pNIPAM-capped Au nanoparticles in NaCl solutions of various concentrations at room temperature. The X-ray data presented in ref 32 for pNIPAM-capped Au nanoparticles in a dilute NaCl solution

(i.e., [NaCl] = 5 mM) under otherwise identical conditions are also used for comparison. In the main text, we refer to the 5 mM NaCl solution as dilute (low concentration) and the 250 and 500 mM NaCl solutions as concentrated (or high concentration). A typical synchrotron X-ray measurement (i.e., reflectivity and grazing-incidence small-angle X-ray scattering (GISAXS)) is performed within a time scale of approximately 30–60 min after varying the salt concentration in the subphase.

#### 3. RESULTS AND DISCUSSION

Previous reports on the salt-induced assembly of polymercapped Au nanoparticles with poly(ethylene glycol) (PEG) and pNIPAM systems demonstrate the versatility of this approach to nanoparticles of various shapes and sizes. 32-34,39,50 It has been reported that the addition of salts to a nonionic water-soluble polymer such as pNIPAM promotes phase separation.<sup>51</sup> The high-salt and low-salt plus polymer liquid/ liquid separation has been recently used to direct polymergrafted nanoparticles in the low-salt phase into one- to threedimensional lattices at the air/water interface as the means to control surface tension. 33,34 As a colloid of pNIPAM-capped Au nanoparticles is driven toward the air/water interface upon the addition of NaCl, it leads to a formation of crystalline 2D lattice. 32,50 However, little is known about the dynamics of the nanoparticles' salt-induced process and the origin of the liquid/ air interfacial crystals. We employed two types of TEM imaging experiments to follow the mechanism of salt-induced assembly of nanoparticles and interfacial lattice formation. First, the dynamic characterization of pNIPAM-capped Au nanoparticle systems in water was carried out with LP-STEM in situ, as shown in the schematics of Figure 1a to analyze the behavior of pNIPAM-capped Au nanoparticles in water with and without NaCl. In the second set of experiments, a microvolume of pNIPAM-capped Au nanoparticles was mixed with NaCl solution to reach a matching concentration of NaCl, and the 2D lattice formed at the air/water interface was collected with a thin flat carbon film and imaged in a dry state. The schematics of this process are presented in Figure 1b. The formation of a salt-induced lateral packing is corroborated by specular X-ray reflectivity (XRR) measurements and GISAXS intensity profiles on the pNIPAM-capped Au nanoparticles at the air/water interface.

3.1. LP-STEM Imaging of pNIPAM-capped Au Nanoparticles in the Presence of NaCl: Liquid/Liquid Phase Separation and the Formation of the Two-Dimensional

**Interfacial Lattice.** Liquid-phase STEM imaging was used to characterize pNIPAM-capped Au nanoparticles in the presence of NaCl. Figure 2a shows a HAADF-STEM image of

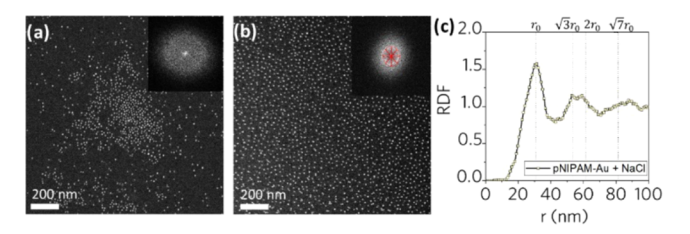


Figure 2. LP-STEM images of pNIPAM-capped Au nanoparticles in water (a) without and (b) with [50 mM] NaCl. The insets show the corresponding FFT. After the salt addition, a nonrigid 2D lattice is formed. (c) Radial distribution of particles with salt addition is consistent with a system exhibiting a hexagonal ordering.

pNIPAM-capped Au nanoparticles without NaCl in liquid cell, with the Au nanoparticles residing in the same focal plane. Random distribution of nanoparticles is evidenced by the lack of discrete spots in the fast Fourier transform (FFT) (shown in the inset). It is worth noting that the assembly of polymergrafted Au nanoparticles into short chains and groups observed after initial short electron beam exposure was ascribed to electron beam effects on the nanoparticle system. At that point, the imaging of aqueous solutions of pNIPAM-capped Au nanoparticles was carried out in the presence of [50 mM] NaCl.

In our initial experiments, the pNIPAM-capped Au nanoparticle system was imaged using two square windows, to achieve a minimal thickness of the liquid layer. The HAADF- STEM image of the salt-colloid solution with [50 mM] NaCl in the liquid phase is shown in Figure 2b. In contrast to Figure 2a, here, the pNIPAM-capped Au nanoparticles formed a two-dimensional nonrigid lattice, as evidenced by the appearance of a sharp ring in the FFT (inset).

The interparticle distance was measured by acquiring the spatial coordinates of all nanoparticles using a Delaunay triangulation. The distance between the near-neighboring nanoparticles was calculated to plot the frequency distribution of nearest neighbor distance and fitted with a Gaussian function to obtain the mean interparticle distance value of 33.7  $\pm$  8.6 nm and the full width at half-maximum (FWHM) = 20.1 nm, as a measure of dispersion. The nanoparticles appeared to reside at the same focal plane. The radial distribution function (RDF) was used to analyze the quality of such a partially ordered lattice. The probability of finding a nanoparticle at a distance r with respect to a particle in the center is plotted in Figure 2c for the system imaged in the presence of a small amount of NaCl. An aqueous solution of pNIPAM-capped Au nanoparticles exhibits a behavior typical of a system with no clear correlation between the positions of individual nanoparticles. Indeed, the RDF assigned is consistent with a nonrigid lattice, as evidenced by the semiperiodicity of the peaks, i.e., partial correlations within a finite correlation range. The correlation between nanoparticles' distance in a 2D hexagonal tiling gives an RDF with peaks at  $r_0$ ,  $\sqrt{3} r_0$ ,  $2r_0$ ,  $\sqrt{7r_0}$ , etc., with  $r_0$  being the distance to the first neighbor. Here, the interparticle distance  $r_0$  between the neighbors, determined to be  $30.8 \pm 4.0$  nm from the first peak of the RDF, is in good agreement with the value found from the near neighbors' distances.

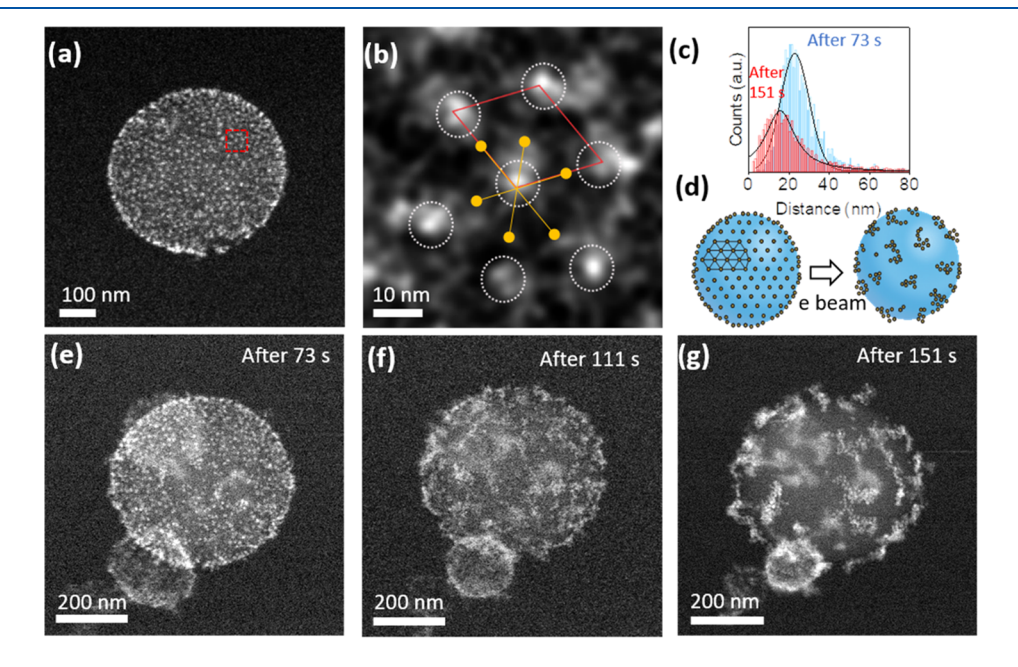


Figure 3. LP-STEM images of pNIPAM-capped Au nanoparticles after addition of 50 mM [NaCl] obtained using two window spacer chips: (a) Formed globular assembly of pNIPAM-capped Au nanoparticles is detected in the liquid phase with the surface-residing nanoparticle's distribution hexagonal lattice as shown in (b) for the area marked in (a). (c) Interparticle distance distribution within the globular assembly measured as the distance to the near neighbors, while LP-STEM imaging after 73 and 151 s of e-beam exposure of structure is shown in (e). (d) Diagram showing the proposed structure and its change as a result of prolonged exposure to the e-beam. (e–g) Beam effect on pNIPAM-capped Au nanoparticles on globular assembly: a slight distortion of the lattice after the first 73 s, notable lattice distortion after 111 s, and full disruption of the interfacial lattice after 151 s of the imaging, respectively. The surface aggregation of nanoparticles and exposure of the surface reveals no substantial change of the globes' structure.

In our consequent experiments carried out upon adding [50 mM] NaCl solution, the pNIPAM-capped Au nanoparticle system was imaged using two spacer window chips, compatible with a fluid flow into the cell and capable of retaining a larger volume of nanoparticle solution. As reported by a number of research groups, while a liquid cell comprised of two 100 nm spacer window chips has a nominal thickness of 200 nm, due to the window bowing, the thickness of a liquid layer is significantly higher, reaching up to 700-800 nm. 40,42,44-46 In the course of our LP-STEM experiments involving two spacer chips, we observed three-dimensional globular nanostructures in excess of 500 nm in diameter. These globular nanostructures were initially detected at the higher concentration of NaCl, when the SiN spacer chip housing the 50 nm thick window membrane was charged with the pNIPAM-capped Au nanoparticles mixed with NaCl solution (see the Methods section). The Supporting Information shows Videos V1 and V2 obtained from such globular assemblies in the liquid phase. A close view of a single globular entity is shown in Figure 3a. The observed globular nanostructures seen "decorated" with Au nanoparticles residing at their surface. A short-range order (SRO) is observed in the zoomed view in Figure 3b from the marked area in Figure 3a. The assembly has a sixfold symmetry closely resembling a hexagonal tiling; the average distance between nanoparticles is shown in blue in Figure 3c with a value for the interparticle distance  $r_0 = 22.9 \pm 7.2$  nm and an full width at half-maximum (FWHM) of 16.8 nm.

The decrease in the interparticle distance compared to the one measured in a nonrigid 2D lattice (Figure 2b) is indicative of stronger interactions among the nanoparticles residing at the surface of the pNIPAM globe compared to those described above. During a continuous electron beam exposure, the semiregular close-packed arrangement of pNIPAM-capped Au nanoparticles is disrupted. Schematics outlining the e-beaminduced distortion of the close-packed nanoparticles decorating the globular structure are shown in Figure 3d. Under the electron beam irradiation, nanoparticles aggregate into short chains or small groups; the initial distribution of nanoparticles is disturbed, although the light contrast of the spherical support remains mostly unchanged, as seen in the sequence in Figure 3e-g. These results are consistent with pNIPAMgrafted Au nanoparticles residing at the surface of the globe filled with the aqueous pNIPAM solution and being affected by the electron beam: the initial interparticle distance of 22.9  $\pm$ 7.2 nm decreases to  $15.6 \pm 9.0$  nm, while the FWHM increases from 16.8 to 20.3 nm, respectively (see Figure 3c red distribution), indicative of the beam-induced clustering of pNIPAM-capped Au nanoparticles, while the distance between the individual groups of clustered nanoparticles is somewhat increased. Here, the lower than 5 nm values in the histogram are attributed to an artifact in the particle location algorithm and do not necessarily represent real physical quantities. The interparticle distances measured from different globes are in good agreement, as described in the Supporting Information, Figure S1 for the globe of the Supporting Information, Video V1. When the identified globes are exposed to the e-beam, their high mobility in both the xy plane and z-direction requires setting the magnification, adjusting for the changes in the focal plane and minimizing sample drift before the actual image acquisition. For the globe presented in Figure 3e-g, this preacquisition time was 73 s. Additional images showing the initial interaction of the globe with the electron beam are

presented and described in detail in the Supporting Information, Figure S2.

We wish to point out that a continuous e-beam illumination delivers a higher cumulative electron dose on the sample resulting in the exposure of nanoparticles to the products of water radiolysis produced by the electron beam, such as hydrated electrons, radicals, and additional highly reactive species, each capable of inducing damage to the Au-decorated surface of transient globes filled with the aqueous pNIPAM solution. 42,45

To illustrate this point, Figure 3e-g shows the images of the same globular structure irradiated for 151 s. Here, after 73 s of imaging, a cumulative dose of around 65 e<sup>-</sup>/Å<sup>2</sup> has been delivered to the system, resulting in a slight distortion in the pNIPAM-Au nanoparticle lattice. The calculations of the beam dose delivered to the specimen in Figure 3 are shown in the Supporting Information. Similar effects were reported for the case of ssDNA-Au lattice using LP-STEM, 52 where subtle changes in the interparticle distance were observed below 80 e<sup>-</sup>/Å<sup>2</sup> due to the dissociation of hydrogen bonds in the DNA base pair. For the case of pNIPAM-Au-decorated globes, a slight distortion of the initial lattice is observed as the imaging progresses from 73 to 111 s, resulting in a complete distortion of the initial structure after delivering a cumulative dose of 172 e<sup>-</sup>/Å<sup>2</sup> after 151 s of continuous imaging, as shown in Figure 3g. The electron beam is likely to degrade the pNIPAM grafted to the Au nanoparticles residing at the surface of the globes, reducing the overall grafting density of the polymer and degrading the quality of the interfacial 2D lattice nanoparticle.

An electron beam damage to the system is expected to include a partial damage to the pNIPAM coronas grafted to the Au nanoparticles, leading to a loss of stability and increase of a nanoparticle mobility, both contributing to nanoparticles aggregation and clustering. The interparticle distance after the e-beam irradiation resembles the minimum distance between particles in liquid without salt, suggestive that the loss of grafting pNIPAM is minor and does not affect the minimum interparticle distance in liquid. Notably, while there is a clear displacement of nanoparticles residing at the surface of the globular entities accompanied by the nanoparticles' aggregation and clustering, overall, the globes appear largely intact and do not exhibit signs of the structural damage associated with the prolonged exposure to the electron beam. In fact, with the exception of the beam-induced aggregation of the surface-bound Au nanoparticles, the structure of the globular entity remains largely intact. Moreover, the variations of contrast of the image are indicative of the presence of Aunanoparticle aggregates formed over the entire surface of the irradiated globe, including the back side of the globe.

Adding NaCl solution to an aqueous sample containing pNIPAM-capped Au nanoparticles introduces ionic kosmotropes (Na and Cl ions) and affects hydrogen bonding in the system. The presence of NaCl furthers the separation between the solution bulk (salt-rich phase) and the excluded volume (pNIPAM-rich phase), manifested as liquid—liquid phase separation. Since NaCl aqueous solution has a slightly higher density compared to that of water at room temperature, the magnitude of the solvent-excluded microvolume effect tends to be more significant. While not widely experimentally observed, such a phenomenon has been reported in the literature for amphiphilic polymeric systems.

Borrowing from the protein terminology, "hydration water" of pNIPAM consists of structured water shells that depend on

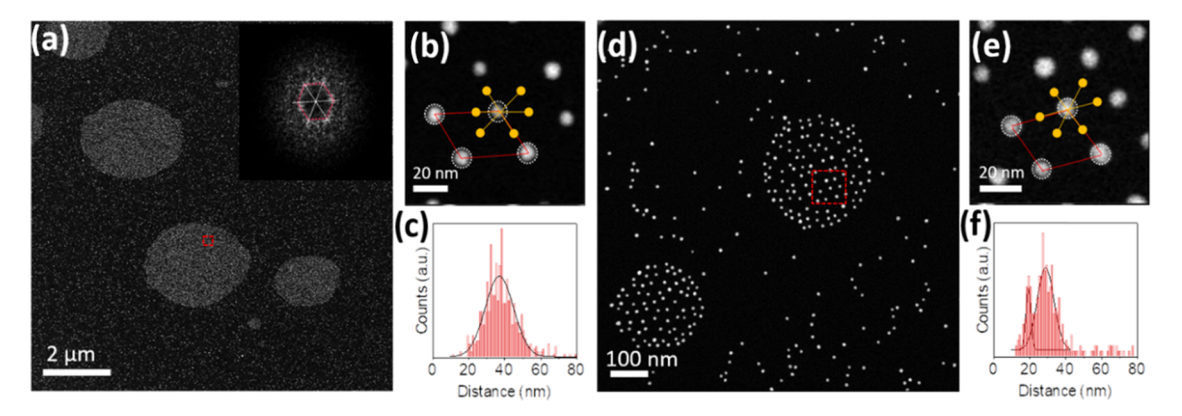


Figure 4. Sample collected from the air/water interface and analyzed in a dry state reveal 2D projection of residual globular aggregates of pNIPAM-capped Au nanoparticles formed upon the addition of NaCl. (a) After adding 50 mM NaCl, large round-shaped aggregates can be seen exhibiting hexagonal symmetry as shown in the inset on the FFT. (b) Zoomed image of the area marked in red in (a) showing a single unit cell and the six closest neighbors. (c) Histogram showing interparticle distance of  $36.9 \pm 8.0$  nm. (d) After adding 500 mM NaCl, smaller circular aggregates of nanoparticles with a short-range hexagonal symmetry are observed. (e) Zoomed-in image of the unit cell of the red square in (d). (f) Histogram of first-neighbor distance showing two peaks corresponding to nanoparticles at the edge and inside the round-shaped nanostructure.

the surface interaction with a slow diffusion dynamics, <sup>56–58</sup> the latter affected by kosmotropic (order-making) additives. <sup>16,17,59–61</sup> Kosmotropes are highly soluble, well-hydrated compounds with strong hydrogen bonds to water molecules. <sup>62</sup> While not a strictly defined kosmotrope added to pNIPAM systems, aqueous NaCl solution is likely to decrease the solubility of hydrophobic pNIPAM, stabilize its aggregates, and lead to the exclusion of bulk solvent from the immediate pNIPAM surrounding, fitting the description of liquid—liquid phase separation. <sup>18,60</sup> In other words, the CGT-induced assembly during the liquid—liquid phase separation of the polymer is likely to stabilize the globular conformations of pNIPAM.

Under this premise, the addition of NaCl favors CGT transition of pNIPAM, leading to the formation of the globular entities filled with the aqueous solution of pNIPAM. Assuming that the grafted polymer inherits the traits of the free polymer, the nanoparticles, grafted to pNIPAM, will follow the saltinduced liquid-liquid phase separation of pNIPAM. The polymer chains grafted onto the Au nanoparticle are facing inwards to minimize their contact with the bulk of the salt-rich solution, leaving the nanoparticles residing at the interface between the two liquids, yielding a surface decorated with Au nanoparticles. While it is not entirely clear whether the LCST of a free polymer is the same as that of a grafter polymer, we assume that the observed globes are formed as a result of saltinduced CGT, and not due to lowering the LCST of pNIPAM in salt solutions, as LCST remains at ~28 °C for a maximum concentration of [500 mM] NaCl, well above the room temperature used in this study.  $^{16,17}$ 

In fact, circular aggregates were also observed while collecting a sample from the air/water interface and imaging in the dry state on a continuous carbon film grid. These circular aggregates serve as a verification that the globular structures observed with the LP-STEM are not an artifact of the liquid-phase imaging, as these structures were detected independently. In the dry state, 2D circular assemblies remain as a product of the 3D Au-decorated buoyant globular structures observed in the liquid phase, escaped to the air/water interface from the NaCl-rich solution. Figure 4a shows a low magnification image of a sample collected with a grid from the surface shortly after the addition of NaCl [50 mM]. The

inset shows the FFT for a single circular feature, which corresponds to a polycrystalline domain with hexagonal symmetry. A zoom-in into the marked area in Figure 4b shows a single unit cell and the six closest neighbors for the particle in the center. The mean interparticle distance calculated from the distribution of near-neighbor distances in Figure 4c is  $36.9 \pm 8.0$  nm (measured from three different regions with more than 2000 particles), with an FWHM of 19.7 nm; the interparticle distance from the circular assemblies is within one standard deviation from the one measured for the soft lattice in the liquid-liquid interface of Figure 2b, indicating no significant change in the interparticle distance from the soft lattice within the liquid and the globes on the air/ water surface. The dispersion of the interparticle distance measured with the FWHM does not change significantly between the dry and liquid states. The circular assemblies have a mean size of 1.7  $\mu$ m measured from around 20 structures in the same sample. We relate the increase in the size of the globes at the air/water interface compared with the one measured in the liquid-liquid interface to the collapse of the 3D globes to 2D circles (nanoparticles are vertically squeezed as one dimension is removed, and such a flattening brings about a slight increase in translation movement into a slight horizontal spread). Figure 4d shows similar flattened circular assemblies of pNIPAM-capped Au nanoparticles collected with a grid after the addition of NaCl [500 mM]. The circular assemblies have a mean diameter of ~263 nm, up to 7 times smaller than those observed at the lower NaCl concentration. Further experimental evidence that allows ruling out the evaporation of the solvent as a possible mechanism of the formation of the 2D lattice in the dry state is discussed in the Supporting Information, Figure S3.

The observed reduction in the size of the circular assemblies with the increase of the salt concentration can be associated with a higher amount of high-density water, which reduces the volume of solvent-excluded pNIPAM-Au nanoparticles. The pNIPAM-capped Au nanoparticles are seemingly residing in the circular nanometer-sized structure, exhibiting a hexagonal symmetry as exemplified in Figure 4e, where an arbitrarily chosen unit cell is displayed, and inspecting the number of closest neighbors for the particle in the center. Here, the interparticles' distances from the histogram of near neighbors

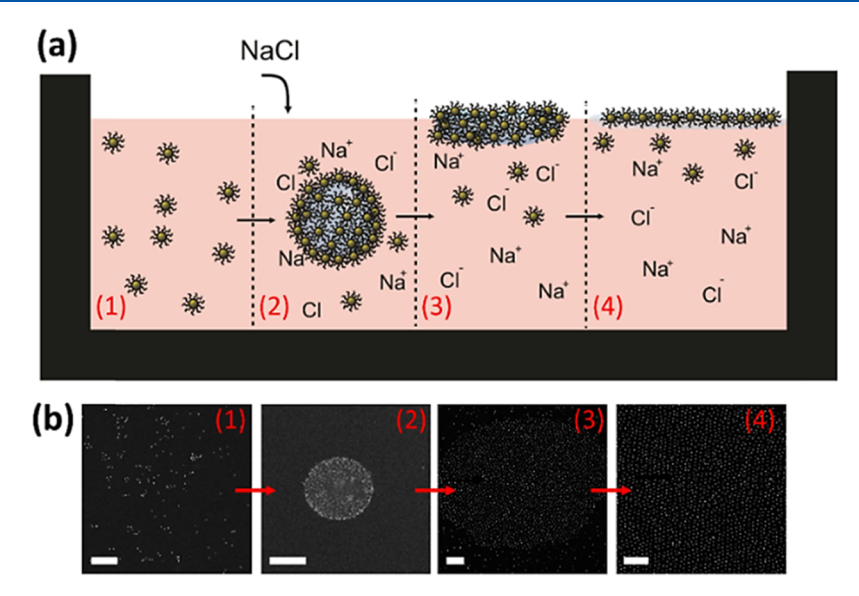


Figure 5. (a) Schematics of the proposed mechanism driving the formation of a 2D lattice of pNIPAM-capped Au nanoparticles in the air/water interface. In the continuous aqueous media, semistable globular structures are formed after the aggregation of salt. The globes are pushed toward the air/water interface, where they flatten and break apart to form the 2D lattice. (b) Illustrative STEM in the proposed mechanism shown in (a), scale bar: 200 nm for all images. For steps (1–2), STEM images of LP-STEM without and with 50 mM NaCl are depicted. The process of salt-induced 2D lattice formation at the air/water interface occurs in the microvolume within seconds, making its observation in real time nearly impossible. The dry-state STEM image of a freshly collected 2D lattice serve as example of the formed of circular motifs at the air/water interface proposed in step (3). Similarly, the dry-state STEM image of a sample collected from a relaxed air/water interface is shown in step (4).

is presented in Figure 4f showing two peaks. The first one corresponds to the nanoparticles in close proximity to the edge of the circle (19.2  $\pm$  3.6 nm, slightly larger than the minimum distance in liquid with an FWHM = 3.3 nm). The second peak is associated with the mean interparticle distance of particles residing inside (28.7  $\pm$  3.7 nm, with an FWHM = 11.1 nm).

The smaller aggregates at the [500 mM] concentration have a narrower distribution, as follows from the decrease in the FWHM. The large standard deviation in the interparticle distance for the sample with [50 mM] makes inconclusive to determine if the concentration of NaCl has any effect on the value of  $r_0$ . Additional experiments to unveil the effect of salt are discussed in the following sections.

As seen, the NaCl concentration plays an important role in the size of the pNIPAM-Au globular assemblies. At low NaCl concentrations, the nanoparticles are driven to self-assembly by the grafted pNIPAM being excluded from the bulk solution to a salt-deficient aqueous phase with a lower density, forming large, micronsize globular structures. At high NaCl concentrations, the excluded volume is reduced, and, therefore, the formed globes are smaller. We hypothesize that the globular assemblies formed in liquid, flatten, and then break apart once they reach the air/water interface.

At low NaCl concentrations, the collapsed giant globes at the surface interact with each other and coalesce to form a more extensive and a somewhat longer-ranged 2D lattice. At high NaCl concentrations, the smaller flattened globes either dissociate into individual nanoparticles or maintain short-range assembly: due to a smaller size of the initial globes, and, consequently, lower surface area, their coalescence into a longrange 2D lattice with a single-crystalline domain is not energetically favorable. Therefore, the system is likely to remain in a patchy, polycrystalline domain state.

The proposed mechanism of formation of the 2D hexagonal lattice at the air/water interface after the addition of NaCl is shown in Figure 5a. We describe this process in four steps:

(1) initial liquid phase of uncorrelated pNIPAM-capped Au nanoparticles in the colloidal system; (2) liquid-liquid phase separation of water-soluble pNIPAM grafted onto the Au nanoparticles from NaCl solution, yielding hexagonally packed Au nanoparticles residing at the interface between the two liquids; (3) lower-denssity Au-decorated globes filled with aqueous pNIPAM solution are pushed upwards to the air/ water interface. While surface tension flattens the globes in a dome-shape, the internal pressure changes, and solvent surface tension ruptures the surface of the globes, leading to their burst and retraction. A thin layer of pNIPAM-capped Au nanoparticles, formed as a result and decorating the surface, quickly retracts and becomes incorporated into the air/water interface. The bursting process can lead to the formation of a pNIPAMcapped Au ring pattern outlining the already existing film of nanoparticles at the interface; (4) nanoparticles rearrange to yield a 2D nanoparticle layer at the air/water interface. The STEM images corresponding to each step of the proposed mechanism are shown in Figure 5b.

The proposed mechanism provides insights into the dynamics of the 2D lattice formation at the air/water interface, afforded by LP-STEM. Understanding the formation mechanism can be used to modify or enhance the salt-induced lattice on the air/water interface. The effect of NaCl concentration on the dispersion and interparticle distance of interfacial nanoparticle lattices collected from the air/water interface in a dry state is discussed below.

**3.2.** Effect of NaCl on the Formation of Interfacial 2D Lattice. As observed, NaCl-induced CGT leads to liquid—liquid phase separation and results in the formation of globular structures, rising to the air/liquid interface, and the concentration of NaCl in solution has a direct effect on the size of the pNIPAM-Au globular structures responsible for forming the 2D lattice in the air/water interface. To explore the effect of NaCl concentration on the quality of interfacial crystals, we collected and analyzed by conventional STEM, the

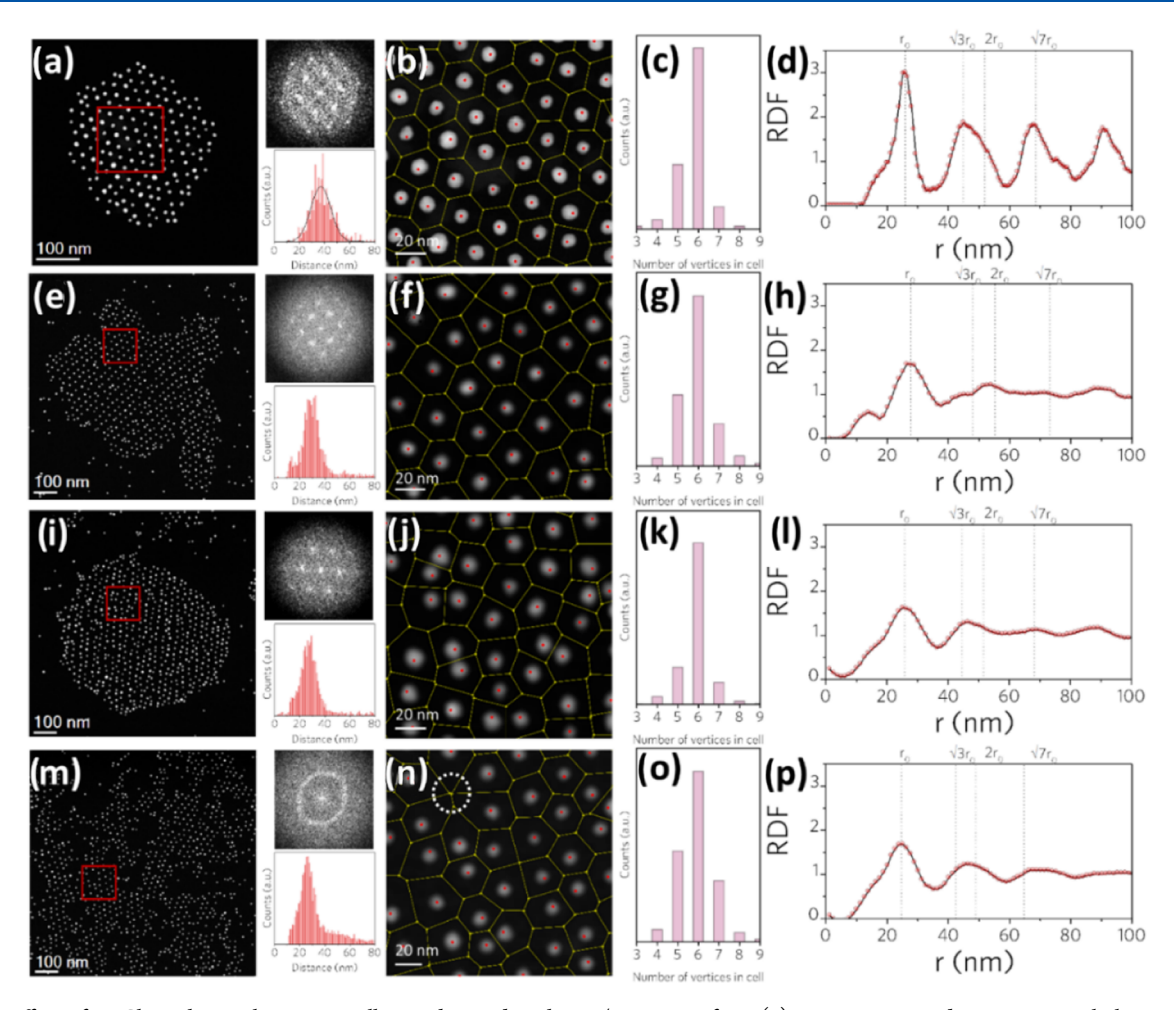


Figure 6. Effect of NaCl on the 2D lattice crystallinity observed at the air/water interface: (a) pNIPAM-capped Au nanoparticle lattice collected after the addition of [5 mM] NaCl. The FFT shows a hexagonal symmetry; interparticle distance distribution shows a narrow distribution. (b) Voronoi's construction from the area marked in red in (a) shows equidistant partition suggesting a crystalline assembly; (c) histogram of the number of vertices in the Voronoi's cells of the image in (a). (d) RDF shows sharp peaks resembling a solid crystal. (e) pNIPAM-capped Au nanoparticle lattice after the addition of [50 mM] NaCl. The FFT and interparticle distance histogram show hexagonal symmetry with a broader distance distribution. (f) Voronoi's construction from the area marked in red in (e) shows a distorted hexagonal lattice; (g) histogram of vertices in the cell still shows hexagonal symmetry. (h) RDF exhibits slightly broadened peaks with lower intensity. A weak peak at ~14 nm is attributed to the individual pNIPAM-capped Au nanoparticles in closer proximity. (i) pNIPAM-capped Au nanoparticle lattice formed after the addition of [250 mM] NaCl. The FFT shows a hexagonal symmetry; the interparticle distance distribution remains wider. (j) Voronoi's cells from the marked area in (i) are highly distorted from the ideal hexagonal shape, although the Voronoi's cells remain mostly hexagonal as evidenced in (k) from the histogram of number of vertices in the cell. (l) RDF shows broadened and weaker-intensity peak consistent with a continuous loss of the crystallinity associated with increased NaCl concentration. (m) pNIPAM-capped Au nanoparticle lattice after the addition of [500 mM] NaCl. The FFT corresponds to polycrystalline domains. Interparticle distance remains similar to previous cases. (n) Respective Voronoi's construction and (o) histogram of cell's vertices show an increment in fivefold symmetry due to the presence of vacancies in the lattice as the once marked in yellow; and (p) radial distribution of the system re

lattice formed at the air/water interface of a microvolume after the addition of NaCl. The summarized results are shown in Figure 6a—d for the 2D lattice formed after addition of NaCl [5 mM], Figure 6e—h for NaCl [50 mM], Figure 6i—l for NaCl [250 mM], and Figure 6m—p for NaCl [500 mM]. For the system with the lower NaCl concentration [5 mM], Figure 6a shows the HAADF-STEM image of a crystalline domain, where the FFT shows a hexagonal symmetry. The mean interparticle distance was found to be  $r_0 = 26.2 \pm 3$  nm with a FWHM = 7.2 nm. Figure 6b shows the Voronoi's construction of the area in red marked in Figure 6a. The hexagonal symmetric partition and equidistance of each Voronoi's cell are a good indication of a crystalline system. A histogram of the number of vertices in the Voronoi's cell shown in Figure 6c counting for the construction among the entire figure is

presented as well. The most common geometry of the Voronoi's cell is the one with six vertices (sixfold symmetry of a hexagonal cell); some four- and five-edge cells are also obtained, and more edge cells are due to boundary effects. Figure 6d shows the RDF with the marked positions expected for a perfect hexagonal lattice. The position and form of the peaks suggest a typical behavior of a "solid" crystalline system. Figure 6e shows the 2D lattice formed after the addition of NaCl [50 mM]. The FFT shows a crystalline hexagonal assembly as well. The interparticle distance is  $r_0 = 29.3 \pm 6.1$  nm with a FWHM = 15.5 nm.

Voronoi's construction in Figure 6f, as well as the increment in the FWHM, suggests a decrease in the crystallinity of the 2D lattice, although the majority of sixfold symmetry is still conserved, since the majority of the Voronoi's cells have six

vertices as evidenced by Figure 6g. Figure 6h shows indeed, a loss in the solid crystalline lattice, observed as a decrease in the intensity and sharpness of the peaks. In the presence of NaCl [250 mM], Figure 6i shows a similar 2D lattice. The FFT of the assembly shows a lower quality hexagonal symmetry with respect to the previous concentrations.

The interparticle distance, in this case, was found to be  $r_0 =$  $27.2 \pm 6.3$  nm with a FWHM = 19.7 nm. The partition of the Voronoi's cells in Figure 6j continues to display distortion in comparison with a perfect hexagonal cell but remaining to be mostly hexagonal Voronoi's cells (Figure 6k). The RDF in Figure 6l shows a behavior that would be the best fit to a "liquid" system. Finally, the case of pNIPAM-capped Au nanoparticles after the addition of [500 mM] of NaCl is presented in Figure 6m. In comparison with lower NaCl concentrations, a larger number of short-range "patches" are observed. The FFT corresponds to polycrystalline domains, although the interparticle distance remains similar to the previous cases with a value of  $r_0 = 26.1 \pm 6.0$  nm with a FWHM = 14.6 nm. The lower FWHM indicates a lower distortion of the mean value of interparticle distance than the cases for 50-250 mM of NaCl.

Figure 6n shows the Voronoi's construction at the short range, where an increase in a number of cells with fivefold symmetry cells of the histogram of vertices in cell in Figure 60 is likely related to the presence of a higher number of vacancies, such as the one marked in white, and can be attributed to the polycrystallinity of the lattice. The radial distribution function in Figure 6p shows no noticeable differences with the other cases of high NaCl concentration. These results provide additional evidence of the shorter-range order at [500 mM] NaCl and are in agreement with the conclusion that by increasing the salt concentration, smaller globular assemblies are formed, yielding the 2D lattice at the air/water interface with smaller domains, and resulting in the formation of a patchy, polycrystalline 2D lattice.

These observations are consistent with the LP-STEM dynamic imaging of the system. pNIPAM-capped Audecorated globes exhibited larger sizes (250–350 nm) at 50 mM NaCl, while pNIPAM-capped Au-decorated globes observed in liquid at 500 mM NaCl exhibited significantly smaller sizes (~150 nm), as shown in the Supporting Information, Videos V1, V2, V3, and V4. A summary of the interparticle distances found for each NaCl concentration is shown in Table 1, calculated from the histograms of the

Table 1. Summary of  $r_0$  and Its FWHM Values Found by Different Methods as a Function of the Salt Concentration

| NaCl<br>(mM) | r <sub>0</sub> (nm) from<br>Delaunay | FWHM (nm)<br>from Delaunay | $r_0$ (nm) from RDF | FWHM (nm)<br>from RDF |
|--------------|--------------------------------------|----------------------------|---------------------|-----------------------|
| 5            | $26.2 \pm 3.0$                       | 7.2                        | $25.6 \pm 2.0$      | 5.8                   |
| 50           | $29.3 \pm 6.1$                       | 15.5                       | $27.8 \pm 4.0$      | 9.9                   |
| 250          | $27.2 \pm 6.3$                       | 19.7                       | $26.0 \pm 4.8$      | 11.2                  |
| 500          | $26.1 \pm 6.0$                       | 14.6                       | $24.6 \pm 4.3$      | 10.1                  |

neighbor's distances in a Delaunay triangulation, and by the position of the first peak in the RDF. The values for the FWHM in each case are also presented.

We observe that the NaCl concentration does not seem to affect the overall interparticle distance, and these values are closer to the one measured in the liquid/liquid phase with LP-STEM for pNIPAM globular structures decorated with Au

nanoparticles (Figure 3a). The values at the air/liquid interface are smaller compared to those observed for the 2D soft lattice in LP-STEM, and after collection of the broken globes at the air/water interface (as introduced in the previous section). We propose a following scenario of interfacial crystal formation:

- (1) After the addition of NaCl to the solution, the CGT drives the initial assembly of pNIPAM into globular structures. The Au nanoparticles, residing at the surface of the pNIPAM-solution-filled globe, and are in close contact, form a hexagonal lattice with a narrow distribution of distances (small value of the FWHM).
- (2) Upon reaching the equilibrium, the globes can merge, their surfaces form continuous lattice at the liquid/liquid interface, and the interparticle distance increases, as the pNIPAM brushes grafted on the Au in liquid are extended. Such a "relaxation" of the lattice also leads to an increase in the dispersion of nanoparticles' distance, marked by a larger value of the FWHM.
- (3) A similar tendency is observed in the circular domains collected at the air/water interface. The collapse of the globes at the air/water surface creates a "relaxed" lattice with extended pNIPAM in between Au nanoparticles, conserving the interparticle distance and distance dispersion of the 2D lattice in the liquid/liquid phase.
- (4) The effect of increasing the NaCl concentration from 5 to 250 mM can be seen in the increase of the dispersion in the interparticle distance (measured by first neighbors and the RDF) while maintaining single-crystalline hexagonal domains.
- (5) Above [250 mM] of NaCl, the formation of smaller globular pNIPAM-capped Au nanoparticle structures in liquid leads to the formation of patchy polycrystalline hexagonal domains. After the system undergoes a transition from single domains to multiple domains, the dispersion in the measure of the distance decreases as the smaller domains become stable short-range hexagonal lattices while keeping the interparticle distance unchanged. Since the single-crystal domain limit is reached above a concentration of [250 mM] of NaCl, we used specular X-ray reflectivity and GISAXS intensity profile measurements to characterize the quality of the single hexagonal domains in the samples with [5] and [250 mM] of salt concentrations, obtained from the air/water interface.

3.3. Grazing-Incidence Small-Angle X-Ray Scattering (GISAXS) and Specular X-Ray Reflectivity (XRR). Specular X-ray reflectivity (XRR) as a function of the momentum transfer along the aqueous surface normal (i.e., Qz) provides the electron density profiles in the vertical z-direction. Figure 7a shows the reflectivity data (R) normalized to the calculated Fresnel reflectivity  $(R_F)$  from the air/water interface for pNIPAM-capped Au nanoparticle suspensions after the addition of [5], [250], and [500 mM] NaCl. The interference pattern in the  $R/R_{\rm F}$  data profiles is reminiscent of the Kiessig fringes typically shown on the reflectivity curves from a homogeneous slab of thickness  $\Delta$ , where the oscillations occur with a period of  $2\pi/\Delta$ . The separation in  $Q_z$  between the first and second maxima in the  $R/R_{\rm F}$  graphs is 0.0675 and 0.0875  $\mathring{A}^{-1}$  for NaCl at a concentration of [250] and [5 mM], respectively. If we approximate the pNIPAM-capped Au nanoparticles at the air/water interface as a uniform layer, based on this simple rule for Kiessig fringes, the thickness of

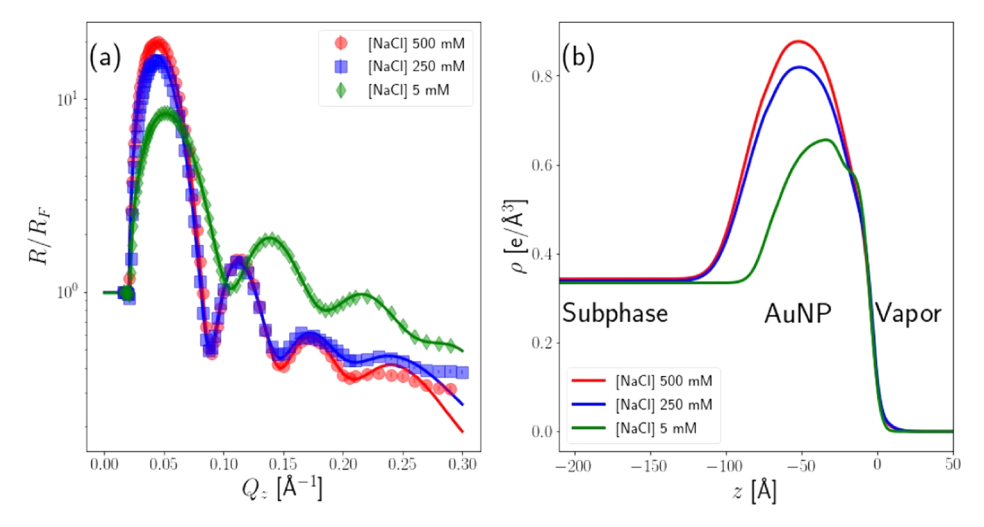


Figure 7. Reflectivity measurements. (a)  $R/R_{\rm F}$  data for pNIPAM-capped Au nanoparticle suspensions at the air/water interface in the presence of NaCl at the concentrations of [500 mM], [250 mM], and [5 mM]. The solid lines are the calculated  $R/R_{\rm F}$  based on the best-fit structural parameters. (b) Corresponding electron density (ED) profiles that best fit the  $R/R_{\rm F}$  data in (a). Three regions can be identified from the ED profiles, namely, the subphase, the Au-enriched interface, and the vapor phase, from left to right.

the film formed by the pNIPAM-capped Au nanoparticles is estimated at 93 and 72 Å for concentrated and diluted NaCl solutions, respectively. The solid lines through the data points in Figure 7a are computed R/R<sub>F</sub> using the Parratt method<sup>63</sup> and best-fit electron density (ED) profiles shown in Figure 7b. The ED profiles exhibit a prominent bell-shaped enhancement with respect to the ED of subphase. Based on the discussion by Wang and co-authors, 39 the ED profile for the diluted NaCl subphase corresponds to the scenario where the pNIPAMcapped Au nanoparticles on the aqueous surface are constrained well on a 2D plane with the center of the Au nanoparticles aligned on the same plane. The thicker pNIPAM-capped Au nanoparticles' layer for the concentrated NaCl subphase suggests a distribution of the particle center in the vertical direction. The amount of the Au nanoparticles on the surface can be estimated knowing the surface electron excess per particle, assuming that the ED contrast between the pNIPAM and the solution is negligible. The surface electron excess density (denoted as  $\Gamma$ ) is defined as  $\Gamma = \int [\rho(z) - \rho_{\rm sol}]$ (z)]dz, where  $\rho(z)$  is the ED profile across the interface and  $\rho_{\rm sol}$  (z) is the ED profile for the solution. Given the ED for pure gold is  $\rho_{Au} = 4.67 \text{ e/Å}^3$  and the diameter of the nominal 10 nm Au nanoparticles is  $D = 88 \pm 8$  Å measured by SAXS, the surface excess ED can be calculated with respect to the subphase solutions.<sup>39</sup> Assuming, on average, a single Au nanoparticle occupies an area A, the expected surface excess ED contributed by a single particle is  $\pi D^3 (\rho_{Au} - \rho_{sol})/6A$ . Based on the  $\Gamma$  obtained from the ED profiles, and the calculated surface excess ED per particle, the area per Au nanoparticle can be obtained as listed in Table 2. The calculation shows that on a concentrated NaCl solution at [250 mM], each surface-bound pNIPAM-capped Au nanoparticle occupies an area 7.7 times of its cross-sectional area  $(\pi D^2/4)$ .

On the other hand, a surface-bound pNIPAM-capped Au nanoparticle on a dilute NaCl solution occupies nearly twice as much surface area. We believe the area per Au nanoparticle at [250 mM] NaCl is almost saturated, as the higher concentration [500 mM] barely changes the reflectivity or GISAXS patterns. Here, the integral width is a measure of the bell-shaped ED enhancement with respect to the subphase by dividing the enhancement area by the maximum ED

Table 2. Structural Parameters Extracted from  $R/R_F$  Data<sup>a</sup>

| NaCl<br>concentration<br>(mM) | surface excess ED (e/Ų) | integral<br>width (Å) | area per Au particle $(\pi D^2/4)$ |
|-------------------------------|-------------------------|-----------------------|------------------------------------|
| 500                           | 36.4                    | 68.2                  | 7.0                                |
| 250                           | 33.0                    | 68.6                  | 7.7                                |
| 5                             | 18.5                    | 57.6                  | 13.7                               |

"Area per pNIPAM-capped Au nanoparticle is given in units of the maximum cross-sectional area of a core Au nanoparticle, i.e.,  $\pi D^2/4$ , D being the diameter and  $D=8.8\pm8$  nm. The relative uncertainty for surface excess electron density (ED) approximately 10%, and the overall relative uncertainty for area per Au particle is approximately 15%.

enhancement. These results are in good agreement with the STEM observations of 2D lattice in a dry state, where the increase in NaCl concentration decreases the quality of the lattice, here evidenced by the decrease in the area for the [250 mM] concentration. The GISAXS data determine the lateral packing of the pNIPAM-Au nanoparticles in the film. Figure 8

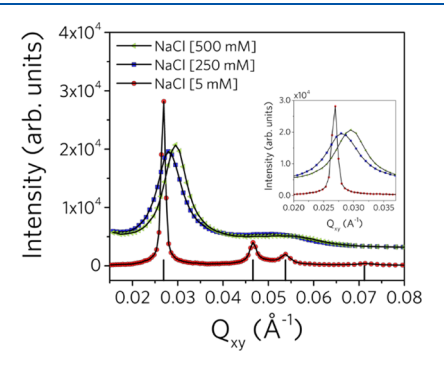


Figure 8. GISAXS intensity profiles integrated over  $Q_z < 0.1 \text{ Å}^{-1}$ . At NaCl [5 mM], the GISAXS profile is the characteristic of sharp Braggreflection peaks, where the vertical lines are calculated position for higher-order Bragg reflections expected from a 2D hexagonal lattice based on the primary peak position. At NaCl [250 mM] and [500 mM] the GISAXS profiles are featured with a broad primary peak and a shoulder at high  $Q_{xy}$ , suggesting a short-range-order (SRO) among surface-bound pNIPAM-Au nanoparticles.

shows the GISAXS intensity profiles that are integrated over  $Q_z$  < 0.1 Å<sup>-1</sup>. For the dilute NaCl concentration of [5 mM], the GISAXS profile exhibits sharp Bragg-reflection peaks. The most intense peak at  $Q_1 = Q_{xy} = 0.0269$  Å<sup>-1</sup> is considered as the primary peak for a 2D hexagonal lattice, and the higher-order reflections are expected at  $Q_{xy}/Q_1 = \sqrt{3}$ ,  $\sqrt{4}$ ,  $\sqrt{7}$ , etc., indicated by the vertical line in Figure 7. In the presence of high-concentration NaCl solution, the GISAXS profile exhibits much broader Bragg-reflection peaks, suggesting a short-range-order (SRO) arrangement of the Au nanoparticles. This is in agreement with the STEM observations.

The primary Bragg-reflection peak can be profile-fit with a Lorentzian function superimposed with a linear baseline, as seen in the inset of Figure 8.

The parameters of the Lorentzian function for the different concentrations are listed in Table 3. By comparing the data in

Table 3. Parameters of the Lorentz Function to Depict the Primary Peak in GISAXS Profiles $^a$ 

| NaCl<br>concentration<br>[mM] | peak<br>position<br>[Å <sup>-1</sup> ] | lattice constant $a_{\rm L}$ [Å] | FWHM<br>[×10 <sup>-3</sup> Å <sup>-1</sup> ] | correlation<br>length [Å] | area per AuNP $[\pi D^2/4]$ |
|-------------------------------|--|----------------------------------|--|---------------------------|-----------------------------|
| 500                           | 0.0295                                 | 248                              | 5.95   | 336                       | 8.77                        |
| 250                           | 0.0282                                 | 257                              | 6.39   | 317                       | 9.42                        |
| 5                             | 0.0268                                 | 269                              | 0.94   | 2127                      | 10.3                        |

"The lattice type is assumed to be two-dimensional hexagonal. Area per pNIPAM-capped Au nanoparticle is given in units of the maximum cross-sectional area of a core Au nanoparticle, i.e.,  $\pi D^2/4$ , D being the diameter and  $D=8.8\pm8$  mm. The relative uncertainty is approximately 2% for the peak position and 10% for the derived area per AuNP.

Tables 2 and 3, the area per Au nanoparticle for [5 mM] NaCl estimated via GISAXS is less than that in terms of reflectivity, indicating that most surface area is covered with crystalline domains of pNIPAM-capped Au nanoparticles.

On the other hand, the area per Au nanoparticle for [250 mM] NaCl estimated via GISAXS is larger than that estimated via reflectivity, suggesting that the ideally 2D planar hexagonal lattice assumption may not hold up. This is further reinforced by the fact that the inferred correlation length is just comparable to the unit cell edge, a typical short-range order. The reflectivity suggests a denser packing. Therefore, combined with the XRR and GISAXS analysis, one can conclude that a high concentration of NaCl results in a denser (smaller), short-range-ordered arrangement of pNIPAMcapped Au nanoparticles within the time scale of the in situ synchrotron X-ray experiments. In contrast, diluted NaCl concentration promotes a crystalline packing of pNIPAMcapped Au nanoparticles with good correlation length persisting over almost 10 units long. This is also consistent with the prior reports on PEG-capped Au nanoparticle surface assembly driven by salts. The increase in subphase salt concentration leads to a denser packing of PEG-capped Au nanoparticles, at the cost of deteriorating crystalline quality.33,34 These results are in line with experimental evidence of pNIPAM brush shrinking induced by NaCl concentration.

The unit cell or lattice parameter measured by GISAXS add insights to the STEM observations. Statistical values over the interparticle distance by image analysis showed no differences between the nanoparticle's distances as the concentration of NaCl increase.

However, as the value of  $r_0$  is measured by the tessellation over the six nearest neighbors after the film is transferred from the air/water interface to a TEM grid, the mean value of the interparticle distance can be larger and more disperse than the lattice parameter value by accounting for distortions created during the transfer. Broadening of the interparticle distance can also be associated with the contribution from a wider range of nanoparticles, in addition to the nearest neighbors. Therefore, both techniques combined allow us to conclude that the NaCl concentration has a slight effect on the interparticle distance forming the 2D hexagonal lattice, but its effect is more predominant in the quality and extension of the crystalline domain, as the dispersion of the distance between nanoparticles becomes larger.

#### 4. CONCLUSIONS

We employed liquid-phase scanning transmission electron microscopy (LP-STEM) imaging to observe a response of a solution containing pNIPAM-capped Au nanoparticles to the presence of NaCl. We explain how the introduction of NaCl prompts the liquid/liquid phase separation process in the system and confines the polymer to a lower-density aqueous phase, manifested by self-assembly of pNIPAM into globular structures excluded from the bulk NaCl solution. pNIPAM chains grafted to Au nanoparticles are facing inwards to minimize the contact with the surrounding salt-rich solution, and the formed nanostructured globes are decorated with Au nanoparticles residing at the interface between the two liquid phases, where pNIPAM-capped Au nanoparticles are hexagonally packed with the interparticle distance of ~23 nm.

The buoyant Au-decorated globes filled with the aqueous solution of pNIPAM escape to the air/water interface and collapse, yielding 2D interfacial crystalline nanoparticle domains. The structure of 2D lattice collected from the air/ water interfaces was examined using conventional STEM imaging. Further, we employed XRR and GISAXS measurements to analyze the quality of air/water interfacial crystals. We describe the effect of NaCl concentration in the interparticle size and crystallinity of the lattice in a dry state. From XRR, the values of interfacial thickness, width, and the population of Au nanoparticles in low and high NaCl concentrated solutions were found. From the ED profiles, we conclude that at low salt concentrations, the pNIPAM-capped Au nanoparticles form a single flat hexagonal layer at the air/ water interface, in good agreement with STEM observations, while at high NaCl concentrations, the layer is corrugated with hexagonal motives. Such a corrugation is consistent with very broad peaks observed in the GISAXS intensity profiles. The increase in salt concentration leads to the formation of a lattice with a shorter lattice parameter (denser) at the expense of the crystalline quality.

The use of liquid-phase scanning transmission electron microscopy and conventional transmission electron microscopy in combination with surface-sensitive scattering techniques afforded unique insights into the salt-induced assembly of nanoparticles capped with amphiphilic polymers. This study provided an opportunity to follow the dynamic process of salt-induced polymer-capped nanoparticle assembly, revealing the origin of two-dimensional crystalline Au nanoparticle lattice formed at the air/water interface and the mechanism of its formation.

#### ASSOCIATED CONTENT

## Supporting Information

The Supporting Information is available free of charge at https://pubs.acs.org/doi/10.1021/acs.jpcc.0c11307.

Description of the cumulative dose delivered to the specimen; and ancillary data, snapshots, and data analysis not included in the main text of the manuscript (PDF)

Video files obtained in the liquid phase from pNIPAM globular assemblies after introducing 50 mM NaCl solution to the system (MP4)

Video files obtained in the liquid phase from pNIPAM globular assemblies after introducing 50 mM NaCl solution to the system (MP4)

video files obtained in the liquid phase from pNIPAM globular assemblies after introducing 500 mM NaCl solution to the system (MP4)

video files obtained in the liquid phase from pNIPAM globular assemblies after introducing 500 mM NaCl solution to the system (MP4)

#### AUTHOR INFORMATION

#### **Corresponding Author**

Tanya Prozorov — Division of Materials Sciences and Engineering, Ames Laboratory, Ames, Iowa 50011, United States; orcid.org/0000-0001-7792-4103; Email: tprozoro@ameslab.gov

#### Authors

Alejandra Londoño-Calderon – Division of Materials Sciences and Engineering, Ames Laboratory, Ames, Iowa 50011, United States

Wenjie Wang — Division of Materials Sciences and Engineering, Ames Laboratory, Ames, Iowa 50011, United States; © orcid.org/0000-0002-7079-1691

Jack J. Lawrence — Department of Physics and Astronomy, Iowa State University, Ames, Iowa 50010, United States

Wei Bu − NSF's ChemMatCARS, University of Chicago, Chicago, Illinois 60637, United States; o orcid.org/0000-0002-9996-3733

David Vaknin — Division of Materials Sciences and Engineering, Ames Laboratory, Ames, Iowa 50011, United States; Department of Physics and Astronomy, Iowa State University, Ames, Iowa 50010, United States; ◎ orcid.org/0000-0002-0899-9248

Complete contact information is available at: https://pubs.acs.org/10.1021/acs.jpcc.0c11307

#### **Author Contributions**

The manuscript was written through the contributions of all authors. All authors have given approval to the final version of the manuscript.

#### Notes

The authors declare no competing financial interest.

### ACKNOWLEDGMENTS

This work was supported by the U.S. Department of Energy (DOE), Office of Science, Basic Energy Sciences, Materials Sciences and Engineering Division. The research was performed at the Ames Laboratory, which is operated for the U.S. Department of Energy by Iowa State University under Contract no. DE-AC02-07CH11358. All TEM-related work

was performed using instruments in the Sensitive Instrument Facility in Ames Laboratory. NSF's ChemMatCARS Sector 15 is principally supported by the Divisions of Chemistry (CHE) and Materials Research (DMR), National Science Foundation, under grant number NSF/CHE-1834750. The use of the Advanced Photon Source, an Office of Science User Facility operated for the U.S. Department of Energy (DOE) Office of Science by Argonne National Laboratory, was supported by the U.S. DOE under Contract no. DE-AC02- 06CH11357. The authors are grateful to Davit Potoyan for helpful discussions.

#### REFERENCES

- (1) Pica, A.; Graziano, G. On the Effect of Sodium Salts on the Coilto-Globule Transition of Poly(N-Isopropylacrylamide). *Phys. Chem. Chem. Phys.* **2015**, *17*, 27750–27757.
- (2) Matsuoka, H.; Moriya, S.; Yusa, S.-i. Fundamental Properties, Self-Assembling Behavior, and Their Temperature and Salt Responsivity of Ionic Amphiphilic Diblock Copolymer Having Poly(N-Isopropylacrylamide) in Aqueous Solution. *Colloid Polym. Sci.* 2018, 296, 77–88.
- (3) Fujita, M.; Hiramine, H.; Pan, P.; Hikima, T.; Maeda, M. Effects of Complementary DNA and Salt on the Thermoresponsiveness of Poly(N-Isopropylacrylamide)-B-DNA. *Langmuir* **2016**, *32*, 1148–1154.
- (4) Alem, H.; Jonas, A. M.; Demoustier-Champagne, S. Poly(N-Isopropylacrylamide) Grafted into Nanopores: Thermo-Responsive Behaviour in the Presence of Different Salts. *Polym. Degrad. Stab.* **2010**, 95, 327–331.
- (5) Naini, C. A.; Thomas, M.; Franzka, S.; Frost, S.; Ulbricht, M.; Hartmann, N. Hofmeister Effect of Sodium Halides on the Switching Energetics of Thermoresponsive Polymer Brushes. *Macromol. Rapid Commun.* **2013**, *34*, 417–422.
- (6) Graziano, G. On the Temperature-Induced Coil to Globule Transition Of poly-N-Isopropylacrylamide in Dilute Aqueous Solutions. *Int. J. Biol. Macromol.* **2000**, *27*, 89–97.
- (7) Graziano, G. On the Mechanism of Cold Denaturation. *Phys. Chem. Chem. Phys.* **2014**, *16*, 21755.
- (8) Sakota, K.; Tabata, D.; Sekiya, H. Macromolecular Crowding Modifies the Impact of Specific Hofmeister Ions on the Coil—Globule Transition of PNIPAM. *J. Phys. Chem. B* **2015**, *119*, 10334–10340.
- (9) Turek, V. A.; Chikkaraddy, R.; Cormier, S.; Stockham, B.; Ding, T.; Keyser, U. F.; Baumberg, J. J. Thermo-Responsive Actuation of a DNA Origami Flexor. *Adv. Funct. Mater.* **2018**, 28, No. 1706410.
- (10) Guo, W.; Lu, C. H.; Qi, X. J.; Orbach, R.; Fadeev, M.; Yang, H. H.; Willner, I. Switchable Bifunctional Stimuli-Triggered Poly-N-Isopropylacrylamide/DNA Hydrogels. *Angew. Chem., Int. Ed.* **2014**, 53, 10134–10138.
- (11) Maeda, Y.; Higuchi, T.; Ikeda, I. Change in Hydration State During the Coil-Globule Transition of Aqueous Solutions of Poly(N-Isopropylacrylamide) as Evidenced by Ftir Spectroscopy. *Langmuir* **2000**, *16*, 7503–7509.
- (12) Pang, X.-c.; Cheng, B.; Cui, S.-x. The Solvent Quality of Water for Poly(N-Isopropylacrylamide) in the Collapsed State: Implications from Single-Molecule Studies. *Chin. J. Polym. Sci.* **2016**, 34, 578–584.
- (13) Park, Y.; Hashimoto, C.; Ozaki, Y.; Jung, Y. M. Understanding the Phase Transition of Linear Poly(N-Isopropylacrylamide) Gel under the Heating and Cooling Processes. *J. Mol. Struct.* **2016**, *1124*, 144–150.
- (14) Wang, X.; Wu, C. Light-Scattering Study of Coil-to-Globule Transition of a Poly(N-Isopropylacrylamide) Chain in Deuterated Water. *Macromolecules* **1999**, 32, 4299–4301.
- (15) Sherman, E.; Haran, G. Coil-Globule Transition in the Denatured State of a Small Protein. *Proc. Natl. Acad. Sci. U.S.A.* **2006**, 103, 11539–11543.
- (16) Zhang, Y.; Furyk, S.; Bergbreiter, D. E.; Cremer, P. S. Specific Ion Effects on the Water Solubility of Macromolecules: Pnipam and the Hofmeister Series. *J. Am. Chem. Soc.* **2005**, *127*, 14505–14510.

- (17) Zhang, Y.; Furyk, S.; Bergbreiter, D. E.; Cremer, P. S. Specific Ion Effects on the Water Solubility of Macromolecules: Pnipam and the Hofmeister Series. *J. Am. Chem. Soc.* **2005**, *127*, 14505–14510.
- (18) Bischofberger, I.; Trappe, V. New Aspects in the Phase Behaviour of Poly-N-Isopropyl Acrylamide: Systematic Temperature Dependent Shrinking of Pnipam Assemblies Well Beyond the LCST. *Sci. Rep.* **2015**, *5*, No. 15520.
- (19) Schild, H. G. Poly(N-Isopropylacrylamide): Experiment, Theory and Application. *Prog. Polym. Sci.* **1992**, *17*, 163–249.
- (20) Huang, F.; Rotstein, R.; Fraden, S.; Kasza, K. E.; Flynnc, N. T. Phase Behavior and Rheology of Attractive Rod-Like Particles. *Soft Matter* **2009**, *5*, 2766–2771.
- (21) Termühlen, F.; Kuckling, D.; Schoenhoff, M. Isothermal Titration Calorimetry to Probe the Coil-to-Globule Transition of Thermoresponsive Polymers. *J. Phys. Chem. B* **2017**, *121*, 8611–8618.
- (22) Halperin, A.; Kroger, M.; Winnik, F. M. Poly(N-Isopropylacrylamide) Phase Diagrams: Fifty Years of Research. *Angew. Chem., Int. Ed.* **2015**, *54*, 15342–15367.
- (23) Ye, X.; Zhu, C.; Ercius, P.; Raja, S. N.; He, B.; Jones, M. R.; Hauwiller, M. R.; Liu, Y.; Xu, T.; Alivisatos, A. P. Structural Diversity in Binary Superlattices Self-Assembled from Polymer-Grafted Nanocrystals. *Nat. Commun.* **2015**, *6*, No. 10052.
- (24) Zhang, H.; Wang, W.; Akinc, M.; Mallapragada, S.; Travesset, A.; Vaknin, D. Assembling and Ordering Polymer-Grafted Nanoparticles in Three Dimensions. *Nanoscale* **2017**, *9*, 8710–8715.
- (25) Dong, D.; Fu, R.; Shi, Q.; Cheng, W. Self-Assembly and Characterization of 2d Plasmene Nanosheets. *Nat. Protoc.* **2019**, *14*, 2691–2706.
- (26) Yi, C.; Yang, Y.; Liu, B.; He, J.; Nie, Z. Polymer-Guided Assembly of Inorganic Nanoparticles. *Chem. Soc. Rev.* **2020**, *49*, 465–508
- (27) Si, K. J.; Chen, Y.; Shi, Q.; Cheng, W. Nanoparticle Superlattices: The Roles of Soft Ligands. *Adv. Sci.* **2018**, *5*, No. 1700179.
- (28) Yun, H.; et al. Symmetry Transitions of Polymer-Grafted Nanoparticles: Grafting Density Effect. *Chem. Mater.* **2019**, *31*, 5264–5273.
- (29) Kim, H. J.; Wang, W.; Bu, W.; Hossen, M. M.; Londoño-Calderon, A.; Hillier, A. C.; Prozorov, T.; Mallapragada, S.; Vaknin, D. Salt Mediated Self-Assembly of Poly(Ethylene Glycol)-Functionalized Gold Nanorods. *Sci. Rep.* **2019**, *9*, No. 20349.
- (30) Nguyen, M.; Felidj, N.; Mangeney, C. Looking for Synergies in Molecular Plasmonics through Hybrid Thermoresponsive Nanostructures. *Chem. Mater.* **2016**, *28*, 3564–3577.
- (31) Kim, H. J.; Hossen, M. M.; Hillier, A. C.; Vaknin, D.; Mallapragada, S. K.; Wang, W. Interfacial and Bulk Assembly of Anisotropic Gold Nanostructures: Implications for Photonics and Plasmonics. ACS Appl. Nano Mater. 2020, 3, 8216–8223.
- (32) Wang, W.; Lawrence, J. L.; Bu, W.; Zhang, H.; Vaknin, D. Two Dimensional Crystallization of Poly(N-Isopropylacrylamide)-Capped Gold Nanoparticles. *Langmuir* **2018**, *34*, 8374–8378.
- (33) Zhang, H.; Wang, W.; Mallapragada, S.; Travesset, A.; Vaknin, D. Ion-Specific Interfacial Crystallization of Polymer-Grafted Nanoparticles. *J. Phys. Chem. C* **2017**, *121*, 15424–15429.
- (34) Zhang, H.; Wang, W.; Mallapragada, S.; Travesset, A.; Vaknin, D. Macroscopic and Tunable Nanoparticle Superlattices. *Nanoscale* **2017**, *9*, 164–171.
- (35) Pérez-Fuentes, L.; Bastos-González, D.; Faraudo, J.; Drummond, C. Effect of Organic and Inorganic Ions on the Lower Critical Solution Transition and Aggregation of Pnipam. *Soft Matter* **2018**, *14*, 7818–7828.
- (36) Chen, J.; Spevacek, J.; Hanykova, L. Nmr Methods to Study Effects of Additives on Phase Separation of Thermoresponsive Polymer. *Macromol. Symp.* **2014**, 339, 24–32.
- (37) Rusu, M.; Wohlrab, S.; Kuckling, D.; Moehwald, H.; Schoenhoff, M. Coil-to-Globule Transition of Pnipam Graft Copolymers with Charged Side Chains: A 1h and 2h Nmr and Spin Relaxation Study. *Macromolecules* **2006**, *39*, 7358–7363.

- (38) Burba, C. M.; Carter, S. M.; Meyer, K. J.; Rice, C. V. Salt Effects on Poly(N-Isopropylacrylamide) Phase Transition Thermodynamics from Nmr Spectroscopy. *J. Phys. Chem. B* **2008**, *112*, 10399–10404.
- (39) Wang, W.; Zhang, H.; Mallapragada, S.; Travesset, A.; Vaknin, D. Ionic Depletion at the Crystalline Gibbs Layer of Peg-Capped Gold Nanoparticle Brushes at Aqueous Surfaces. *Phys. Rev. Mater.* **2017**, *1*, No. 076002.
- (40) Evans, J. E.; Jungjohann, K. L.; Browning, N. D.; Arslan, I. Controlled Growth of Nanoparticles from Solution with in Situ Liquid Transmission Electron Microscopy. *Nano Lett.* **2011**, *11*, 2809–2813.
- (41) Chee, S. W.; Anand, U.; Bisht, G.; Tan, S. F.; Mirsaidov, U. Direct Observations of the Rotation and Translation of Anisotropic Nanoparticles Adsorbed at a Liquid-Solid Interface. *Nano Lett.* **2019**, 19, 2871–2878.
- (42) Woehl, T. J.; Prozorov, T. The Mechanisms for Nanoparticle Surface Diffusion and Chain Self-Assembly Determined from Real-Time Nanoscale Kinetics in Liquid. *J. Phys. Chem. C* **2015**, *119*, 21261–21269.
- (43) Powers, A. S.; Liao, H.-G.; Raja, S. N.; Bronstein, N. D.; Alivisatos, A. P.; Zheng, H. Tracking Nanoparticle Diffusion and Interaction During Self-Assembly in a Liquid Cell. *Nano Lett.* **2017**, *17*, 15–20.
- (44) Touve, M. A.; Carlini, A. S.; Gianneschi, N. C. Self-Assembling Peptides Imaged by Correlated Liquid Cell Transmission Electron Microscopy and Maldi-Imaging Mass Spectrometry. *Nat. Commun.* **2019**, *10*, No. 4837.
- (45) Woehl, T. J.; Moser, T.; Evans, J. E.; Ross, F. M. Electron-Beam-Driven Chemical Processes During Liquid Phase Transmission Electron Microscopy. *Mater. Res. Bull.* **2020**, *45*, 746–753.
- (46) Lee, W. C.; Kim, B. H.; Choi, S.; Takeuchi, S.; Park, J. Liquid Cell Electron Microscopy of Nanoparticle Self-Assembly Driven by Solvent Drying. *J. Phys. Chem. Lett.* **2017**, *8*, 647–654.
- (47) Cepeda-Perez, E.; Doblas, D.; Kraus, T.; de Jonge, N. Electron Microscopy of Nanoparticle Superlattice Formation at a Solid-Liquid Interface in Nonpolar Liquids. *Sci. Adv.* **2020**, *6*, No. eaba1404.
- (48) Lee, J.; Nakouzi, E.; Song, M.; Wang, B.; Chun, J.; Li, D. Mechanistic Understanding of the Growth Kinetics and Dynamics of Nanoparticle Superlattices by Coupling Interparticle Forces from Real-Time Measurements. *ACS Nano* **2018**, *12*, 12778–12787.
- (49) Schlossman, M. L.; Synal, D.; Guan, Y.; Meron, M.; Shea-McCarthy, G.; Huang, Z.; Acero, A.; Williams, S. M.; Rice, S. A.; Viccaro, P. J. A Synchrotron X-Ray Liquid Surface Spectrometer. *Rev. Sci. Instrum.* 1997, 68, 4372–4384.
- (50) Minier, S.; Kim, H. J.; Zaugg, J.; Mallapragada, S. K.; Vaknin, D.; Wang, W. Poly(N-Isopropylacrylamide)-Grafted Gold Nanoparticles at the Vapor/Water Interface. *J. Colloid Interface Sci.* **2021**, 585, 312–319.
- (51) Liu, G.; Cheng, H.; Yan, L.; Zhang, G. Study of the Kinetics of the Pancake-to-Brush Transition of Poly(N-Isopropylacrylamide) Chains. *J. Phys. Chem. B* **2005**, *109*, 22603–22607.
- (52) Sutter, P.; Zhang, B.; Sutter, E. Radiation Damage During in Situ Electron Microscopy of DNA-Mediated Nanoparticle Assemblies in Solution. *Nanoscale* **2018**, *10*, 12674–12682.
- (53) Ianiro, A.; Wu, H.; van Rijt, M. M. J.; Vena, M. P.; Keizer, A. D. A.; Esteves, A. C. C.; Tuinier, R.; Friedrich, H.; Sommerdijk, N. A. J. M.; Patterson, J. P. Liquid–Liquid Phase Separation During Amphiphilic Self-Assembly. *Nat. Chem.* **2019**, *11*, 320–328.
- (54) Penfold, N. J. W.; Yeow, J.; Boyer, C.; Armes, S. P. Emerging Trends in Polymerization-Induced Self-Assembly. *ACS Macro Lett.* **2019**, *8*, 1029–1054.
- (55) Figg, C. A.; Simula, A.; Gebre, K. A.; Tucker, B. S.; Haddleton, D. M.; Sumerlin, B. S. Polymerization-Induced Thermal Self-Assembly (Pitsa). *Chem. Sci.* **2015**, *6*, 1230–1236.
- (56) Russo, D. The Impact of Kosmotropes and Chaotropes on Bulk and Hydration Shell Water Dynamics in a Model Peptide Solution. *Chem. Phys.* **2008**, 345, 200–211.

- (57) Hunt, N. T.; Kattner, L.; Shanks, R. P.; Wynne, K. The Dynamics of Water-Protein Interaction Studied by Ultrafast Optical Kerr-Effect Spectroscopy. *J. Am. Chem. Soc.* **2007**, *129*, 3168.
- (58) Raschke, T. M. Water Structure and Interactions with Protein Surfaces. Curr. Opin. Struct. Biol. 2006, 16, 152–159.
- (59) Lever, M.; Blunt, J. W.; Maclagan, R. G. A. R. Some Ways of Looking at Compensatory Kosmotropes and Different Water Environments. *Comp. Biochem. Physiol., Part A: Mol. Integr. Physiol.* **2001**, *130*, 471.
- (60) Bischofberger, I.; Calzolari, D. C. E.; De Los Rios, P.; Jelezarov, I.; Trappe, V. Hydrophobic Hydration of Poly-N-Isopropyl Acrylamide: A Matter of the Mean Energetic State of Water. *Sci. Rep.* **2014**, *4*, No. 4377.
- (61) Casanova-Morales, N.; Alavi, Z.; Wilson, C. A. M.; Zocchi, G. Identifying Chaotropic and Kosmotropic Agents by Nanorheology. *J. Phys. Chem. B* **2018**, *122*, 3754–3759.
- (62) http://www1.lsbu.ac.uk/water/kosmotropes chaotropes.html.
- (63) Als-Nielsen, J.; McMorrow, D. Elements of Modern X-Ray Physics; John Wiley & Sons: England, 2011.
- (64) Pecharsky, V. K.; Zavalij, P. Y. Fundamentals of Power Diffraction and Structural Characterization of Materials; Springer, 2009.
- (65) Christau, S.; Moeller, T.; Genzer, J.; Koehler, R.; von Klitzing, R. Salt-Induced Aggregation of Negatively Charged Gold Nanoparticles Confined in a Polymer Brush Matrix. *Macromolecules* **2017**, 50, 7333–7343.